

1 **Agreement between different linear-combination modelling algorithms for**
2 **short-TE proton spectra**

3 Helge J. Zöllner^{1,2,*}, Michal Považan^{1,2}, Steve C. N. Hui^{1,2}, Sofie Tapper^{1,2}, Richard A. E. Ed-
4 den^{1,2}, Georg Oeltzschner^{1,2}

5 ¹ *Russell H. Morgan Department of Radiology and Radiological Science, The Johns Hopkins*
6 *University School of Medicine, Baltimore, MD, United States*

7 ² *F. M. Kirby Research Center for Functional Brain Imaging, Kennedy Krieger Institute, Balti-*
8 *more, MD, United States*

9

10 ***Corresponding author:**

11 Georg Oeltzschner, Ph.D.

12 Division of Neuroradiology, Park 367G

13 The Johns Hopkins University School of Medicine

14 600 N Wolfe St

15 Baltimore, MD 21287

16 goeltzsl@jhmi.edu

17

18 *Word count: 4808*

19 *Figure count: 6*

20 *Table count: 2*

21 *Keywords: MRS, linear-combination modelling, short-echo-time spectra, LCM*

22 **Abstract**

23 Purpose

24 Short-TE proton MRS is used to study metabolism in the human brain. Common analysis meth-
25 ods model the data as linear combination of metabolite basis spectra. This large-scale multi-site
26 study compares the levels of the four major metabolite complexes in short-TE spectra estimated
27 by three linear-combination modelling (LCM) algorithms.

28 Methods

29 277 short-TE spectra from a recent multi-site study were pre-processed with the Osprey soft-
30 ware. The resulting spectra were modelled with Osprey, Tarquin and LCMModel, using the same
31 three vendor-specific basis sets (GE, Philips, and Siemens) for each algorithm. Levels of total N-
32 acetylaspartate (tNAA), total choline (tCho), myo-inositol (mI), and glutamate+glutamine (Glx)
33 were quantified with respect to total creatine (tCr).

34 Results

35 Group means and CVs of metabolite estimates agreed well for tNAA and tCho across vendors
36 and algorithms, but substantially less so for Glx and mI, with mI systematically estimated lower
37 by Tarquin. The cohort mean correlation coefficient for all pairs of LCM algorithms across all
38 datasets and metabolites was $\overline{\mathbf{R}^2}=0.39$, indicating generally only moderate agreement of indi-
39 vidual metabolite estimates between algorithms. There was a significant correlation between lo-
40 cal baseline amplitude and metabolite estimates (cohort mean $\overline{\mathbf{R}^2}=0.10$).

41 Conclusion

42 While mean estimates of major metabolite complexes broadly agree between linear-combination
43 modelling algorithms at group level, correlations between algorithms are only weak-to-moderate,
44 despite standardized pre-processing, a large sample of young, healthy and cooperative subjects,
45 and high spectral quality. These findings raise concerns about the comparability of MRS studies,
46 which typically use one LCM software and much smaller sample sizes.

47 Introduction

48 Proton MRS allows in-vivo research studies of metabolism^{1,2}. Single-voxel MR spectra from the
49 human brain are frequently acquired using PRESS localization³, and can be modelled to esti-
50 mate metabolite levels. Accurate modelling is hampered by poor spectral resolution at clinical
51 field strengths, and for short-echo-time spectra, metabolite signals overlap with a broad back-
52 ground consisting of fast-decaying macromolecule and lipid signals. Linear-combination model-
53 ling (LCM) of the spectra maximizes the use of prior knowledge to constrain the model solution,
54 and is recommended by recent consensus⁴. LCM algorithms model spectra as a linear combina-
55 tion of (metabolite and macromolecular (MM)) basis functions, and typically also include terms
56 to account for smooth baseline fluctuations.

57

58 Several LCM algorithms are available to quantify MR spectra (**Table 1** describes some of the
59 most widely used: Osprey⁵, INSPECTOR⁶, Tarquin⁷, AQSES⁸, Vespa⁹, QUEST¹⁰, LCMoel¹¹).
60 The implementations (open-source vs. compiled ‘black-box’), modelling approaches (modelling
61 domain and baseline model), and their licensure practices are diverse.

62

63 **Table 1.** Overview of linear-combination modelling algorithms. The domain (time TD or fre-
64 quency FD) of modelling and the baseline model approach are specified. *Citations re-
65 ported from Google Scholar on July 29, 2020.

Name	Modelling Domain, Baseline approach	Cost	Code Availability	Published	Cita-tions*
Osprey	FD, spline baseline	free	open	2020	1
INSPECTOR	FD, 1 st -order polynomial	free	open	2018	0
Tarquin	TD, smooth baseline	free	open	2011	252
AQSES (jMRUI)	TD, spline baseline	free	closed	2007	140
Vespa	FD, wavelet baseline	free	open	2006	68
QUEST (jMRUI)	TD, spline baseline	free	closed	2004	305
LCMoel	FD, spline baseline	\$13,300	closed	1992	3454

66

67 Surprisingly few studies have compared the performance of different LCM algorithms. Cross-
68 validation of quantitative results has almost exclusively been performed in the context of bench-
69 marking new algorithms against existing solutions. In-vivo comparisons are often limited to

70 small sample sizes, whether analyzing spectra from animal models^{7,12,13} or human subjects^{7,8,12}.
71 To the best of our knowledge, two exceptions compared the LCM performance of different algo-
72 rithms in rat brain¹⁴ and human body¹⁵, respectively. Most studies report good agreement be-
73 tween results from different algorithms, inferring this from group-mean comparisons, or observ-
74 ing that differences between clinical groups are consistent regardless of the algorithm ap-
75 plied^{14,16}. Correlations of estimates from different algorithms are rarely reported; however, a high
76 correlation between LCM and Tarquin results was found in the rat brain at ultra-high field¹⁴.
77 Despite the fact that LCM has been used to analyze thousands of studies (Table 1), a comprehen-
78 sive assessment of the agreement between the algorithms is lacking, and the relationship between
79 the choice of model parameters and quantitative outcomes is poorly understood. To begin to ad-
80 dress this gap, we conducted a large-scale comparison of short-TE in-vivo MRS data using three
81 LCM algorithms with standardized pre-processing. While recent expert consensus recommends
82 using measured MM background spectra, data for different sequences are not broadly available
83 or integrated in LCM software. This manuscript investigates current common practice, and there-
84 fore all models included simulated MM basis functions. We compared group-mean quantifica-
85 tion results of four major metabolite complexes from each LCM algorithm, performed between-
86 algorithm correlation analyses, and investigated local baseline power and creatine modelling as
87 potential sources of differences between the algorithms.

88 **Methods**

89 **Participants & acquisition**

90 277 single-voxel short-TE PRESS datasets from healthy volunteers acquired in a recent multi-
91 site-study¹⁷ were included in this analysis. Data were acquired at 25 sites (with up to 12 subjects
92 per site) on scanners from three different vendors (GE: 8 sites with n = 91; Philips: 10 sites with
93 n = 112; and Siemens: 7 sites with n = 74) with the following parameters: TR/TE = 2000/35 ms;
94 64 averages; 2, 4 or 5 kHz spectral bandwidth; 2048-4096 data points; acquisition time = 2.13
95 min; 3×3×3 cm³ voxel in the medial parietal lobe. Reference spectra were acquired with similar
96 parameters, but without water suppression and 8-16 averages (for more details, please refer to
97 ¹⁷). Data were saved in vendor-native formats (GE P-files, Philips .sdatt, and Siemens TWIX). In
98 the initial study¹⁸, written informed consent was obtained from each participant and the study
99 was approved by local institutional review boards. Anonymized data were shared securely and
100 analyzed at Johns Hopkins University with local IRB approval. Due to site-based data privacy
101 guidelines, only a subset of these data (GE: 7 sites with n = 79; Philips: 9 sites with n = 100; and
102 Siemens: 4 sites with n = 48) is publicly available¹⁹.

103

104 **Data pre-processing**

105 MRS data were pre-processed in Osprey⁵, an open-source MATLAB toolbox, following recent
106 peer-reviewed pre-processing recommendations², as summarized in **Figure 1A**. First, the ven-
107 dor-native raw data were loaded, including the metabolite (water-suppressed) data and unsup-
108 pressed water reference data. Second the raw data were pre-processed into averaged spectra. Re-
109 ceiver-coil combination²⁰ and eddy-current correction²¹ of the metabolite data were performed
110 using the water reference data. Individual transients in Siemens and GE data were frequency-
111 and-phase aligned using robust spectral registration²², while Philips data had been averaged on
112 the scanner. After averaging the individual transients, the residual water signal was removed
113 with a Hankel singular value decomposition (HSVD) filter²³. For Siemens spectra, an additional
114 pre-phasing step was introduced by modelling the signals from creatine and choline-containing
115 compounds at 3.02 and 3.20 ppm with a double Lorentzian model and applying the inverted
116 model phase to the data. This step corrected a zero-order phase shift in the data arising from the

117 HSVD water removal, likely because the Siemens water suppression introduced asymmetry to
 118 the residual water signal. Finally, the pre-processed spectra were exported in .RAW format.

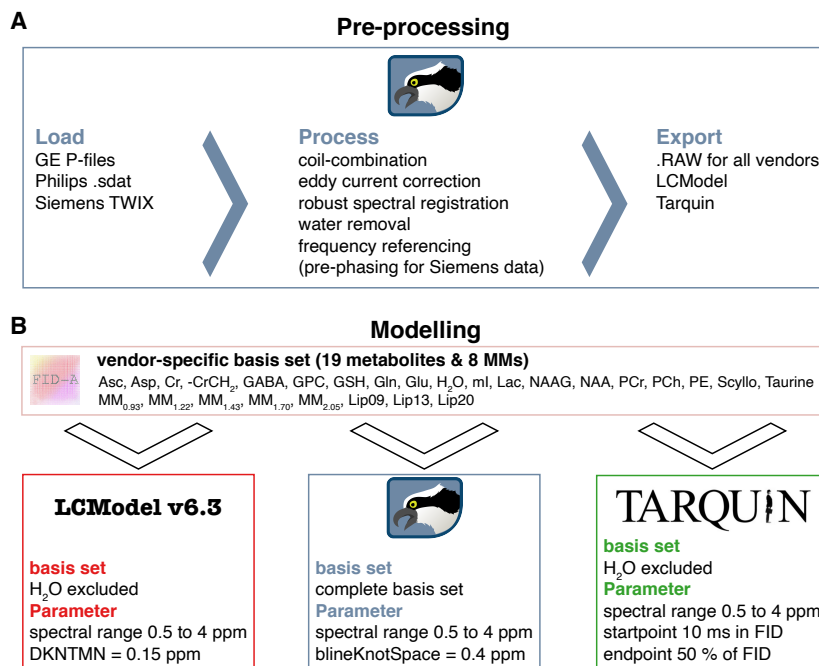


Figure 1. Overview of the MRS analysis pipeline. (A) Pre-processing pipeline implemented in Osprey including ‘OspreyLoad’ to load the vendor-native spectra, ‘OspreyProcess’ to process the raw data and to export the averaged spectra. (B) Modelling of the averaged spectra with details of the basis set and parameters of each LCM (LCModel, Osprey, and Tarquin).

119 Data modelling

120 Fully localized 2D density-matrix simulations implemented in the MATLAB toolbox FID-A²⁴
 121 with vendor-specific refocusing pulse information, timings, and phase cycling were used to gen-
 122 erate three vendor-specific basis sets (GE, Philips, and Siemens) including 19 spin systems:
 123 ascorbate, aspartate, Cr, negative creatine methylene (-CrCH₂), γ -aminobutyric acid (GABA),
 124 glycerophosphocholine (GPC), glutathione, glutamine (Gln), glutamate (Glu), water (H₂O), myo-
 125 inositol (ml), lactate, NAA, N-acetylaspartylglutamate (NAAG), phosphocholine (PCh), PCr,
 126 phosphoethanolamine, scyllo-inositol, and taurine. The -CrCH₂ term is a simulated negative cre-
 127 atine methylene singlet at 3.95 ppm, included as a correction term to account for effects of water
 128 suppression and relaxation. It is not included in the tCr model, which is used for quantitative ref-
 129 erencing.

130 8 additional Gaussian basis functions were included in the basis set to simulate broad macromol-
131 ecules and lipid resonances²⁵ (simulated as defined in section 11.7 of the LCMoDel manual²⁶):
132 MM_{0.94}, MM_{1.22}, MM_{1.43}, MM_{1.70}, MM_{2.05}, Lip09, Lip13, Lip20. The Gaussian amplitudes were
133 scaled relative to the 3.02 ppm creatine CH₃ singlet in each basis set (details in **Supplementary**
134 **Information 1**). Finally, to standardize the basis set for each algorithm, basis sets were stored as
135 .mat files for use in Osprey and as .BASIS-files for use in LCMoDel and Tarquin. In the follow-
136 ing paragraphs, each LCM algorithm investigated in this study is described briefly (for details,
137 please refer to the original publications^{5,7,11}).

138 LCMoDel v6.3

139 The LCMoDel (6.3-0D) algorithm¹¹ models data in the frequency-domain. First, time-domain
140 data and basis functions are zero-filled by a factor of two. Second, frequency-domain spectra are
141 frequency-referenced by cross-correlating them with a set of delta functions representing the ma-
142 jor singlet landmarks of NAA (2.01 ppm), Cr (3.02 ppm), and Cho (3.20 ppm). Third, starting
143 values for phase and linebroadening parameters are estimated by modelling the data with a re-
144 duced basis set containing NAA, Cr, PCh, Glu, and mI, with a smooth baseline. Fourth, the final
145 modelling of the data is performed with the full basis set, regularized lineshape model and base-
146 line, with starting values for phase, linebroadening, and lineshape parameters derived from the
147 previous step. Model parameters are determined with a Levenberg-Marquardt^{27,28} non-linear
148 least-squares optimization implementation that allows bounds to be imposed on the parameters.
149 Metabolite amplitude bounds are defined to be non-negative, and determined using a non-nega-
150 tive linear least-squares (NNLS) fit at each iteration of the non-linear optimization. Amplitude
151 ratio constraints on macromolecule and lipid amplitude, as well as selected pairs of metabolite
152 amplitudes (e.g. NAA+NAAG), are defined as in Osprey and Tarquin. LCMoDel constrains the
153 model with three additional regularization terms. Two of these terms penalize a lack of smooth-
154 ness in the baseline and lineshape models using the second derivative operator, preventing unrea-
155 sonable baseline flexibility and lineshape irregularity. The third term penalizes deviations of the
156 metabolite Lorentzian linebroadening and frequency shift parameters from their expected values.

157

158 Osprey

159 The Osprey (1.0.0) algorithm⁵ adopts several key features of the LCMoDel and Tarquin algo-
160 rithms. Osprey follows the four-step workflow of LCMoDel including zero-filling, frequency

161 referencing, preliminary optimization to determine starting values, and final optimization over
162 the real part of the frequency-domain spectrum. The model parameters are zero- and first-order
163 phase correction, global Gaussian linebroadening, individual Lorentzian linebroadening, and in-
164 dividual frequency shifts, which are applied to each basis function before Fourier transformation.
165 The frequency-domain basis functions are then convolved with an arbitrary, unregularized line-
166 shape model to account for deviations from a Voigt profile. The length of this lineshape model is
167 estimated during the initial referencing step and set to 2.5 times the FWHM estimate. The line-
168 shape model is normalized, so that the convolution does not impact the integral of basis func-
169 tions.

170 The spline baseline is constructed from cubic B-spline basis functions, including one additional
171 knot outside either end of the user-specified fit range, as in LCMoel. In contrast to LCMoel,
172 the baseline curvature is not regularized. Therefore, the baseline knot spacing is set to 0.15 ppm
173 for preliminary modelling step with a reduced basis set and increased to 0.4 ppm for the final full
174 model. Similar to LCMoel, model parameters are determined with a Levenberg-Marquardt^{27,28}
175 non-linear least-squares optimization algorithm and a NNLS fit to determine the non-negative
176 metabolite amplitudes at each step of the non-linear optimization.

177 Tarquin

178 Tarquin (4.3.10)⁷ uses a four-step approach in the time domain to model spectra. First, residual
179 water is removed using singular value decomposition. Second, the global zero-order phase is de-
180 termined by minimizing the difference between the magnitude and the real spectra in the fre-
181 quency domain. Third, zero-filling to double the number of points and frequency referencing are
182 performed, as in the other algorithms. This step also estimates a starting value for the Gaussian
183 linebroadening used in the fourth step, the final modelling. The model includes common Gauss-
184 ian linebroadening, individual Lorentzian linebroadening, individual frequency-shifts, and zero-
185 and first-order phase correction factors applied in the frequency domain.

186 Optimization is performed in the time domain with a constrained non-linear least-squares Leven-
187 berg-Marquardt solver, allowing bounds and constraints on the parameters. In addition, the range
188 of time-domain datapoints is limited by removing the first 10 ms of the FID, so as to omit the
189 fast-decaying macromolecule and lipid signals. Finally, the baseline is estimated in the frequency
190 domain by convolving the model residual with a Gaussian filter with a width of 100 points.

191

192 Model parameters

193 The parameters chosen for each tool are summarized in **Figure 1B**. The fit range was limited to
194 0.5 to 4 ppm in all tools to reduce effects of differences in water suppression techniques. For the
195 baseline handling, the default parameters were chosen, i.e. bLineKnotSpace = 0.4 ppm for Os-
196 prey, DKNMNT = 0.15 ppm for LCMoel, and an FID range from 10 ms to 50% of the FID for
197 Tarquin.

198

199 Quantification, visualization, and secondary analyses

200 The four major metabolite complexes tNAA (NAA + NAAG), tCho (GPC + PCh), mI, and Glx
201 (Glu + Gln) were quantified as basis-function amplitude ratios relative to total creatine (tCr = Cr
202 + PCr). Since the primary purpose was to compare performance of the core LCM algorithms, no
203 additional relaxation correction or partial volume correction was performed.

204

205 Model visualizations were generated with the *OspreyOverview* module, which allows LCMoel
206 and Tarquin results files (.coord and .txt) to be imported. For each algorithm, the visualization
207 includes site-mean spectra, cohort-mean spectra (i.e. the mean of all spectra), and site- and co-
208 hort-mean modelling results (complete model, spline baseline, spline baseline + MM compo-
209 nents, and the separate models of the major metabolite complexes).

210 Three secondary analyses included a linewidth and SNR analysis, as well as the investigation of
211 local baseline power and creatine modelling as potential sources of differences between the algo-
212 rithms (details in **Supplementary Information 2**).

213

214 Data analysis

215 Quantitative metabolite estimates (tNAA/tCr, tCho/tCr, mI/tCr, Glx/tCr) were statistically ana-
216 lyzed and visualized using R²⁹ in RStudio (Version 1.2.5019, RStudio Inc.). The functions are
217 publicly available³⁰. The supplemental materials with MATLAB- and R-files, example LCMoel
218 control files (one for each vendor), and Tarquin batch-files for this study are publicly available³¹.
219 The results from each LCM algorithm were imported into R with the *spant* package³².

220 Distribution analysis

221 The results are presented as raincloud plots³³ and Pearson's correlation analysis using the
222 *ggplot2* package³⁴. The raincloud plots include individual data points, boxplots with median and

223 25th/75th percentiles, a smoothed distribution, and mean \pm SD error bars to identify systematic
224 differences between the LC algorithms. In addition, the coefficient of variation ($CV = SD/mean$)
225 and the mean $\overline{CV} = \frac{(CV_{tNAA} + CV_{tCho} + CV_{tIns} + CV_{tGlx})}{4}$ across all four metabolites of each algorithm are
226 calculated.

227 Correlation analysis

228 The correlation analysis featured different levels, including pair-wise correlations between algo-
229 rithms, as well as correlations between baseline power and metabolite estimates of each algo-
230 rithm. The pair-wise correlation on the global level (black R^2), as well as within-vendor correla-
231 tions (color-coded R^2) with different color shades for different sites are reported. Furthermore,
232 mean $\overline{R^2}$ for each pair-wise correlation (e.g. Osprey vs LCModel) and metabolite, estimated by
233 row or column means e.g. $\overline{R^2} = \frac{(R_{tNAA}^2 + R_{tCho}^2 + R_{tIns}^2 + R_{tGlx}^2)}{4}$, and a cohort mean $\overline{R^2}$ (across all pair-
234 wise correlations) are calculated. For the correlations, no correction for multiple testing was ap-
235 plied. The cohort mean $\overline{R^2}$ was used to identify global associations across all correlation analy-
236 sis, while the mean $\overline{R^2}$ allowed the identification of algorithm-specific (row means) and metab-
237 olite-specific (column means) interactions across all correlation analysis. Associations between
238 the outcome of specific algorithms were identified by the pair-wise correlation analysis (R^2).
239 Vendor-specific effects were identified by differentiating between global level and within-vendor
240 correlations.

241 Statistical analysis

242 In the statistical analysis, the presence of significant differences in the mean and the variance of
243 the metabolite estimates was assessed. Global metabolite estimates were compared between al-
244 gorithms with parametric tests, following recommendations for large sample sizes³⁵. Differences
245 of variances were tested with Fligner-Killeen's test with a post-hoc pair-wise Fligner-Killeen's
246 test and Bonferroni correction for the number of pair-wise comparisons. Depending on whether
247 variances were different or not, an ANOVA or Welch's ANOVA was used to compare means
248 with a post-hoc paired t-test with equal or non-equal variances, respectively.

249

250 **Results**

251 All 277 spectra were successfully processed, exported, and quantified with the three LCM algo-
252 rithms; no modelled spectra were excluded from further analysis.

253 Summary and visual inspection of the modelling results

254 A site-level averaged summary of the 277 spectra is shown in **Figure 2A, B and C**, for analyses
255 in LCModel, Osprey, and Tarquin, respectively. The averaged data, models and residuals for
256 each of the 25 sites are color-coded by vendor. The cohort-mean of all analyses for each vendor
257 is shown in **Figure 2D, E and F** (GE, Philips and Siemens, respectively). Data, models and re-
258 siduals are color-coded by algorithm.

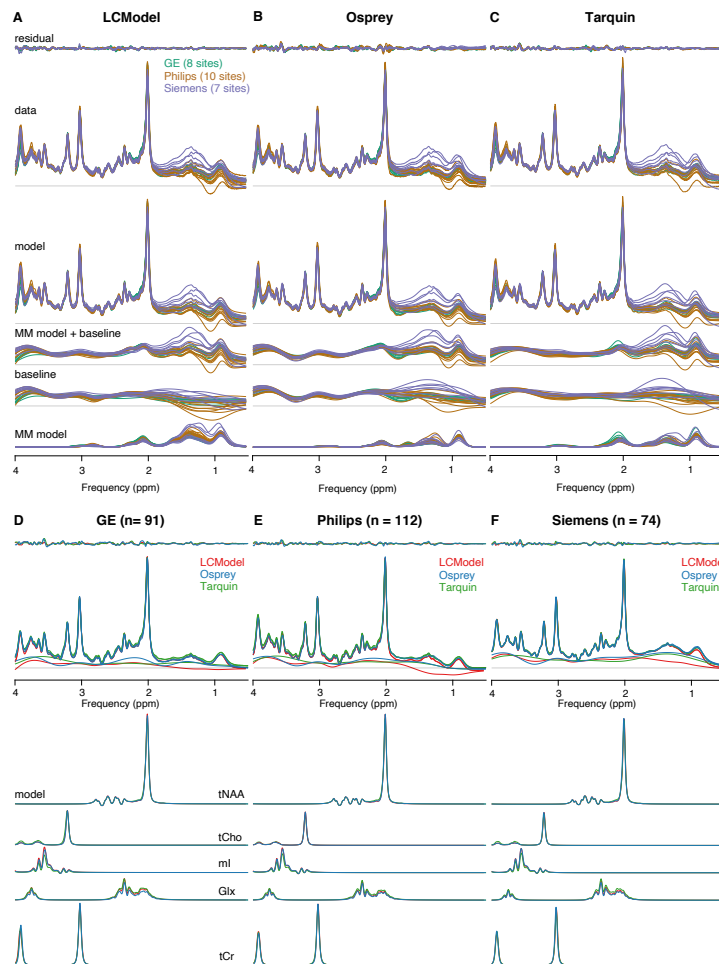


Figure 2. Summary of the modelling results. (A–C) site-level averaged residual, data, model, MM model + baseline, baseline and MM model for each LCM algorithm, color-coded by vendor. (D–F) cohort-mean residual, data, model, MM model + baseline, and metabolite models for each vendor, color-coded by LCM algorithm.

259

260 In general, the phased spectra and models agreed well between vendors for all algorithms. Com-
261 paring the algorithms, notable differences in spectral features in the estimated baseline models
262 appeared between 0.5 and 1.95 ppm (degree of variability: Osprey > LCModel > Tarquin) and
263 between 3.6 and 4 ppm (degree of variability: LCModel > Osprey > Tarquin) (as shown in **Fig-**
264 **ure 2A-C**).

265 Cohort-mean spectra and models agreed well across all vendors and algorithms (**Figure 2D-F**).
266 The greatest differences in the spectral features of the baseline between algorithms occur be-
267 tween 0.5 and 1.95 ppm, with closer agreement between Osprey and Tarquin than with
268 LCModel. The amplitude of the residual over the whole spectral range is highest for Osprey, and
269 similar for Tarquin and LCModel.

270 NAA linewidth was significantly lower ($p < 0.001$) for Philips (6.3 ± 1.3 Hz) compared to GE
271 (7.3 ± 1.5 Hz), while no differences in the linewidth were found for the other comparisons (Sie-
272 mens 6.6 ± 2.4 Hz). SNR was significantly higher for Siemens (285 ± 72) compared to both
273 other vendors ($p < 0.001$) and significantly higher ($p < 0.001$) for Philips (226 ± 58) compared to
274 GE (154 ± 37).

275

276 Metabolite level distribution

277 **Table 2** – Metabolite level distribution. Mean, standard deviation and coefficient of variation
 278 (CV) of each metabolite-to-creatinine ratio, listed by algorithm and vendor as well as global
 279 summary values. Asterisks indicate significant differences (adjusted $p < 0.01 = **$ and adjusted
 280 $p < 0.001 = ***$ or #### or ''') in the mean (for the metabolite ratios) or the variance (for the CV)
 281 compared to the algorithm in the next row (LCModel vs Osprey = ** or ***, Osprey vs Tarquin
 282 = ####, and Tarquin vs LCModel = ''').

	[metabolite] / [tCr] (mean ± SD)			
	tNAA	tCho	mI	GlX
GE				
LCModel	1.48 ± 0.12	0.19 ± 0.02	0.85 ± 0.10	1.75 ± 0.25
Osprey	1.47 ± 0.10	0.18 ± 0.02	0.78 ± 0.09	1.42 ± 0.17
Tarquin	1.48 ± 0.11	0.22 ± 0.03	0.57 ± 0.07	2.05 ± 0.22
Philips				
LCModel	1.38 ± 0.10	0.17 ± 0.02	0.81 ± 0.08	1.46 ± 0.14
Osprey	1.50 ± 0.12	0.18 ± 0.02	0.86 ± 0.10	1.34 ± 0.16
Tarquin	1.40 ± 0.12	0.16 ± 0.03	0.60 ± 0.09	1.78 ± 0.19
Siemens				
LCModel	1.52 ± 0.19	0.19 ± 0.02	0.83 ± 0.09	1.65 ± 0.31
Osprey	1.54 ± 0.12	0.19 ± 0.02	0.89 ± 0.06	1.45 ± 0.14
Tarquin	1.50 ± 0.15	0.18 ± 0.03	0.65 ± 0.07	2.04 ± 0.19
global				
LCModel	1.45 ± 0.15***	0.18 ± 0.02	0.83 ± 0.09	1.45 ± 0.15***
Osprey	1.50 ± 0.12###	0.18 ± 0.02	0.84 ± 0.09###	1.50 ± 0.12###
Tarquin	1.46 ± 0.14	0.18 ± 0.04	0.60 ± 0.08''''	1.93 ± 0.24''''
	CV (SD/mean)			
	tNAA	tCho	mI	GlX
GE				
LCModel	7.9%	12.9%	11.8%	14.2%
Osprey	6.9%	9.7%	11.1%	11.8%
Tarquin	7.5%	11.7%	11.2%	10.8%
Philips				
LCModel	7.2%	10.6%	9.9%	9.7%
Osprey	8.0%	10.0%	11.8%	11.9%
Tarquin	8.8%	19.8%	15.2%	10.7%
Siemens				
LCModel	12.4%	13.4%	10.8%	18.7%
Osprey	8.0%	11.1%	6.9%	10.0%
Tarquin	10.1%	14.3%	10.5%	9.3%
global				
LCModel	10.0%	13.2%**	10.9%	16.4%***
Osprey	7.8%	10.4%###	11.7%###	11.8%###
Tarquin	9.3%	20.5%''''	13.6%	12.3%

283
 284 The tCr ratio estimates and CVs of the four metabolites are summarized in **Table 2**. Distributions
 285 and group statistics are visualized in **Figure 3**, with the four rows corresponding the three ven-
 286 dors and a cohort summary across all datasets.

287

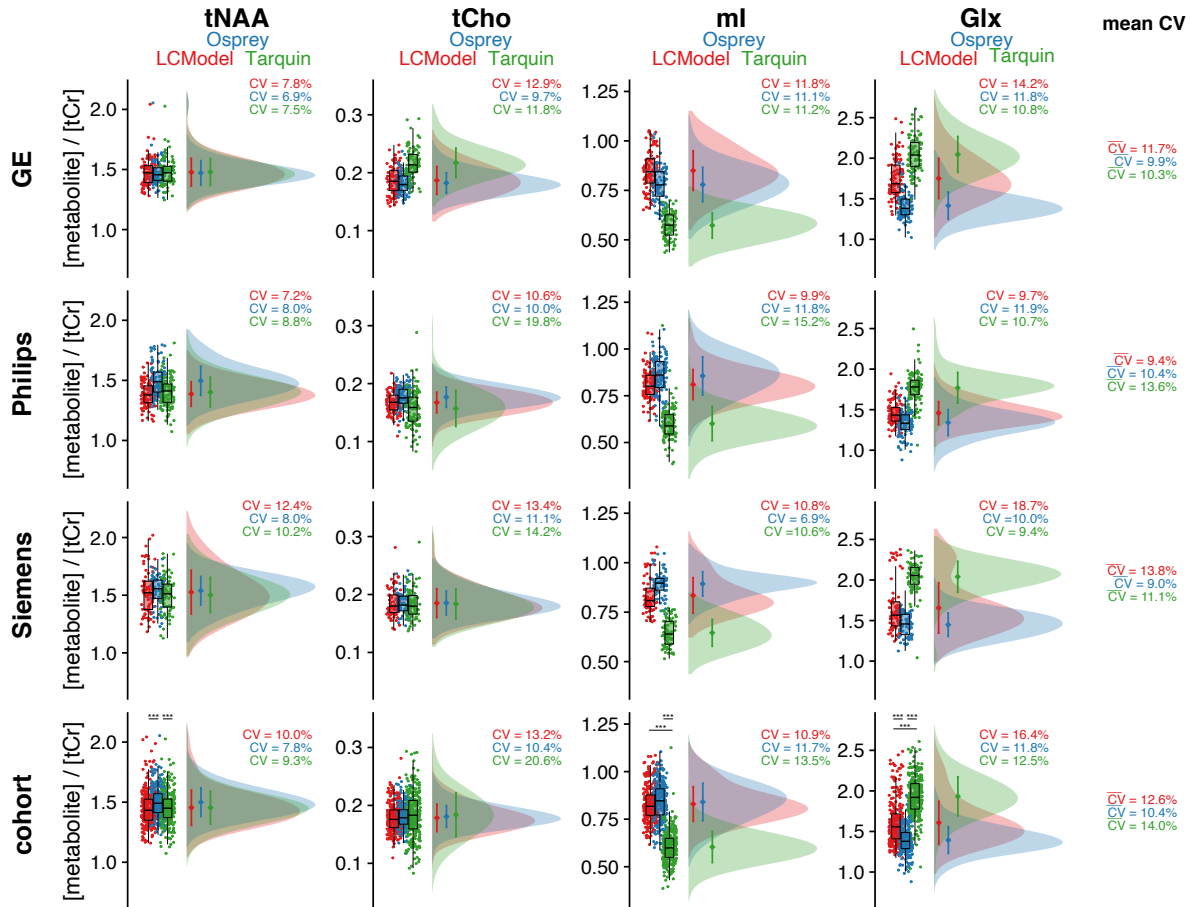


Figure 3. – Metabolite level distribution. Raincloud plots of the metabolite estimates of each LCM algorithm (color-coded). The four metabolites are reported in the columns, and the three vendors in rows, with a cohort summary in the last row. The coefficient of variation is reported for each distribution, as well as a mean \overline{CV} reported in the last column, which is calculated across each row. Asterisks indicate significant differences (adjusted $p < 0.001 = ***$).

288

289 Between-algorithm agreement was greatest for the group means and CVs of tNAA and tCho.

290 The cohort-mean CV was lowest for Osprey (10.4%), followed by LCMModel (12.6%) and Tar-

291 quin (14.0%). Group means and CVs for tNAA are relatively consistent. As a result, the cohort-

292 mean tNAA/tCr was 1.45 ± 0.15 for LCMModel, 1.50 ± 0.12 for Osprey, and 1.45 ± 0.14 for Tar-

293 quin, with significant differences between Osprey and both other LCM algorithms.

294 Cohort means for tCho showed a high agreement between all algorithms. The global CV of tCho

295 estimates was significantly higher for Tarquin compared to both other algorithms, and signifi-

296 cantly lower for Osprey compared to LCMModel. Global tCho/tCr was 0.18 ± 0.02 for LCMModel,

297 0.18 ± 0.02 for Osprey, and 0.18 ± 0.04 for Tarquin.

298 For mI, group means and CVs were comparable for Osprey and LCModel, while Tarquin esti-
299 mates were lower by about 25%. Global CVs were significantly lower for Osprey compared to
300 Tarquin, while no significant differences in the CV were found for the other comparisons. Global
301 mI/tCr was 0.83 ± 0.09 for LCModel, 0.84 ± 0.09 for Osprey, and 0.60 ± 0.08 for Tarquin, with
302 significant mean differences between all Tarquin and both other algorithms.
303 Group means and CVs for Glx were comparable between Osprey and LCModel, while estimates
304 were about 30% higher in Tarquin. Global CV was significantly lower for Osprey compared to
305 both other algorithms. Global Glx/tCr was 1.45 ± 0.15 for LCModel, 1.50 ± 0.12 for Osprey, and
306 1.93 ± 0.24 for Tarquin, with significant differences between all algorithms. Mean \overline{CVs} , esti-
307 mated by the row-mean, were between 9.0 and 13.8% for all algorithms and vendors.

308

309 Correlation analysis: pairwise comparison between LCM algorithms

310 The correlation analysis for each metabolite and algorithm pair is summarized in **Figure 4**. $\overline{R^2}$
311 for each algorithm pair and metabolite are reported in the corresponding row and column, re-
312 spectively.

313 The cohort-mean $\overline{R^2} = 0.39$ suggests an overall moderate agreement between metabolite esti-
 314 mates from different algorithms. The agreement between algorithms, estimated by the row-mean

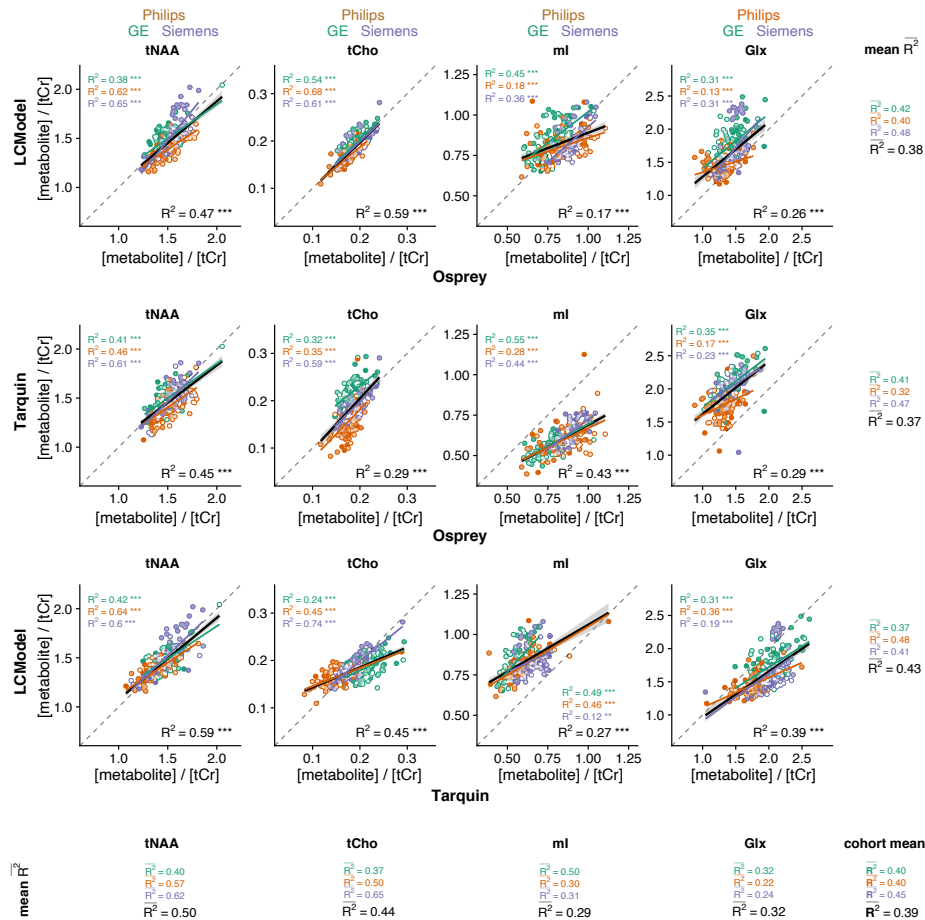


Figure 4. Pairwise correlational comparison of algorithms. LCMoDel and Osprey are compared in the first row, Tarquin and Osprey in the second row, and LCMoDel and Tarquin in the third row. Each column corresponds to a different metabolite. Within-vendor correlations are color-coded; global correlations are shown in black. The $\overline{R^2}$ values are calculated along each dimension of the grid with mean R^2 for each metabolite and each correlation. A cohort-mean $\overline{R^2}$ value is also calculated across all twelve pair-wise correlations. Asterisks indicate significant correlations ($p < 0.01 = **$ and $p < 0.001 = ***$).

315 $\overline{R^2}$, was highest for Tarquin-vs-LCModel ($\overline{R^2} = 0.43$), followed by Osprey-vs-LCModel ($\overline{R^2}$
316 $= 0.38$), and Osprey-vs-Tarquin ($\overline{R^2} = 0.37$).

317 The agreement between algorithm for each metabolite, estimated by the column-mean $\overline{R^2}$, was
318 highest for tNAA ($\overline{R^2} = 0.50$), followed by tCho ($\overline{R^2} = 0.44$), Glx ($\overline{R^2} = 0.32$), and mI ($\overline{R^2} =$
319 0.29). The cohort-mean $\overline{R^2}$ for each vendor was higher for Siemens ($\overline{R^2} = 0.45$) than for GE
320 ($\overline{R^2} = 0.40$) and Philips ($\overline{R^2} = 0.40$).

321

322 While the within-metabolite mean $\overline{R^2}$ (average down the columns in Figure 4) are comparable
323 between vendors, there is substantially higher variability of the R^2 values with increasing granu-
324 larity of the analysis. **Supplementary Information 3** includes an additional layer of correlations
325 at the site level.

326

327 Correlation analysis: baseline and metabolite estimates

328 The correlation analysis between local baseline power and metabolite estimates for each algo-
329 rithm is summarized in **Figure 5**. The cohort-mean $\overline{R^2} = 0.10$ suggests that overall, there is an
330 association between local baseline power and metabolite estimates, that is weak but statistically
331 significant. The influence of baseline on metabolite estimates differs between metabolites, as re-
332 flected by the column-mean $\overline{R^2}$ which was lowest for tCho ($\overline{R^2} = 0.04$) and tNAA ($\overline{R^2} =$
333 0.06), and higher for mI ($\overline{R^2} = 0.13$) and Glx ($\overline{R^2} = 0.18$). The global baseline correlations all
334 had negative slope, except for tCho estimates of Tarquin.

335 The mean $\overline{R^2}$ across metabolites for each algorithm, calculated as the row mean, were low for
 336 all algorithms with LCMoDel ($\overline{R^2} = 0.17$) showing a greater effect than Tarquin ($\overline{R^2} = 0.08$)
 337 and Osprey ($\overline{R^2} = 0.06$). Comparing between vendors, the cohort-mean $\overline{R^2}$ was higher for GE
 338 ($\overline{R^2} = 0.15$) and Siemens ($\overline{R^2} = 0.14$) than for Philips ($\overline{R^2} = 0.05$) spectra.

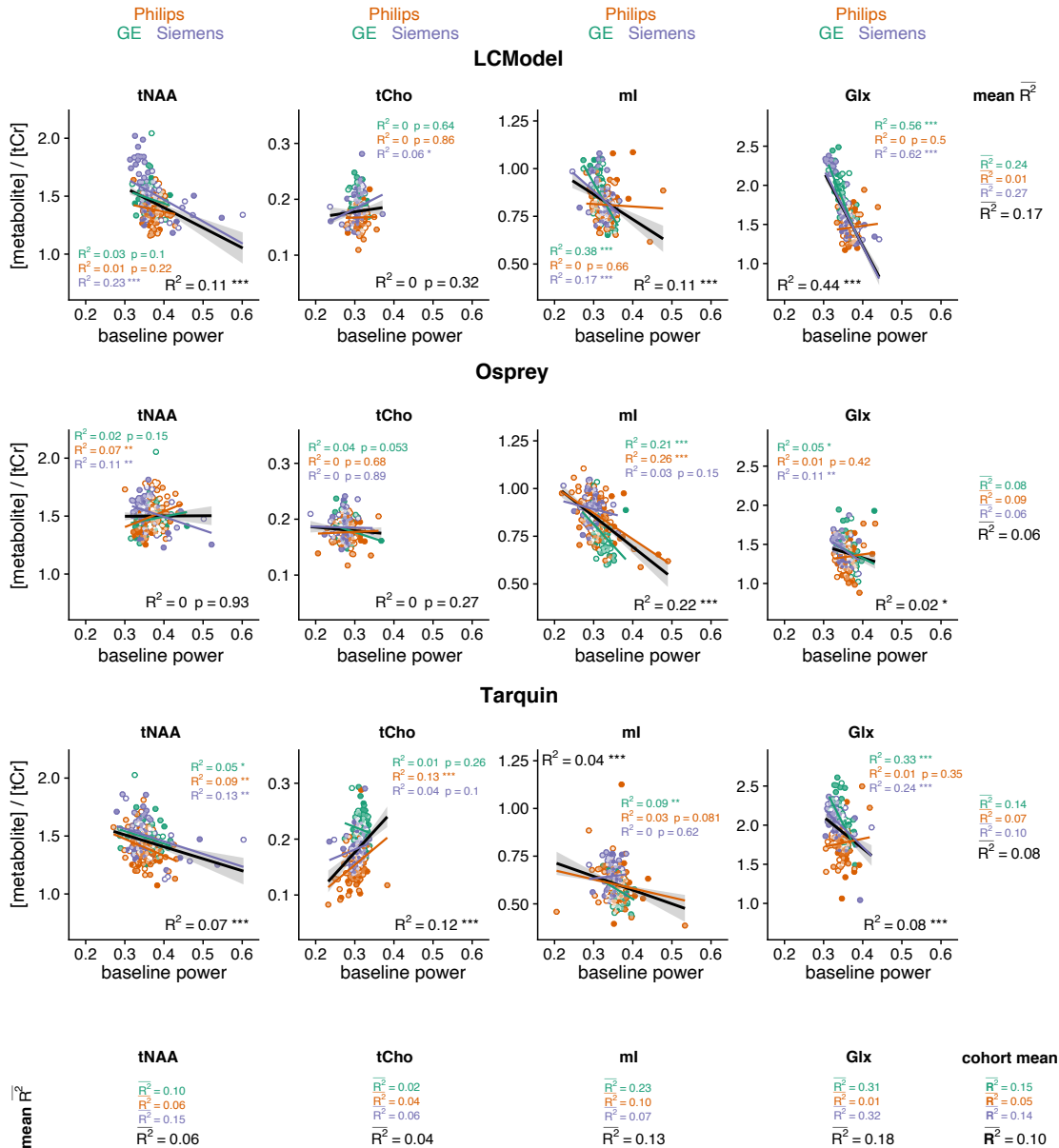


Figure 5. Correlation analysis between metabolite estimates and local baseline power for each algorithm, including global (black) and within-vendor (color-coded) correlations. The mean $\overline{R^2}$ values are calculated along each dimension of the grid for each metabolite and each algorithm. Similarly, a cohort-mean $\overline{R^2}$ value is calculated across all twelve pair-wise correlations. Asterisks indicate significant correlations ($p < 0.05 = *$, $p < 0.01 = **$, $p < 0.001 = ***$).

339 Variability of total creatine models

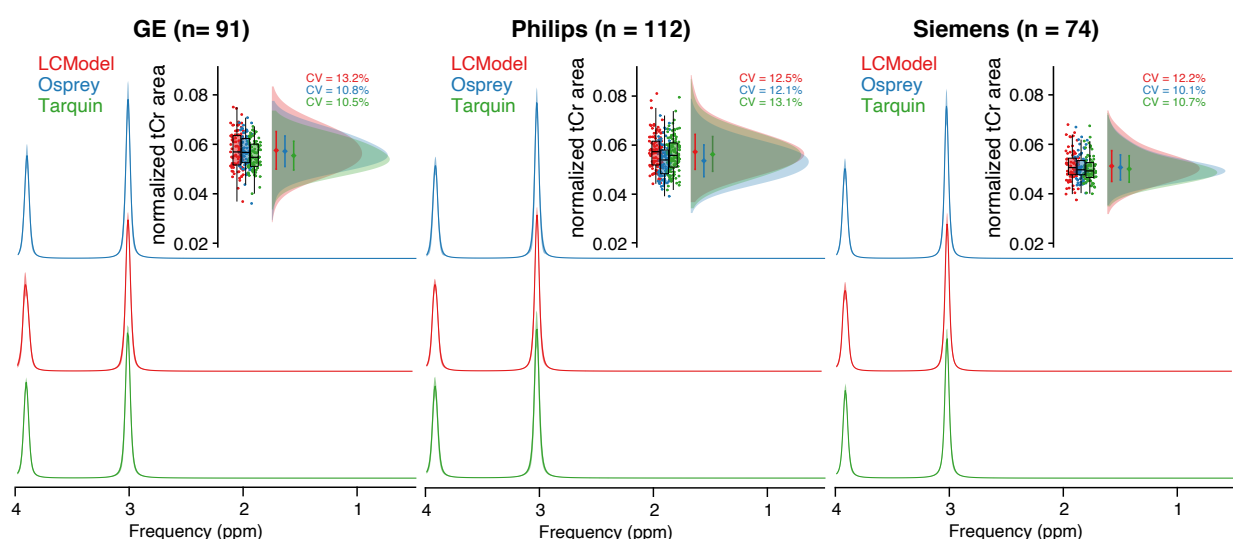


Figure 6. Variability of tCr models. Mean models \pm standard deviation (shaded areas) are presented column-wise by vendor and color-coded by LCM algorithm. The distribution and CV of the areas under the models are inset.

340 Mean tCr model spectra (\pm one standard deviation) are summarized in **Figure 6** for each vendor
341 and LCM algorithm, along with distribution plots of the area under the model.
342 The agreement in mean and CV is greatest between Osprey and Tarquin for all vendors, while
343 tCr areas for LCMoDel appear slightly higher. Differences in water suppression are accounted for
344 with the $-\text{CrCH}_2$ correction term, which is not included in the tCr model used for quantitative ref-
345 erencing.

346 **Discussion**

347 We have presented a three-way comparison of LCM algorithms applied to a large dataset of
348 short-TE in-vivo human brain spectra. The aims at the onset were to compare metabolite esti-
349 mates obtained with different LCM algorithms, as applied in the literature, and to identify poten-
350 tial sources of differences between the algorithms. The major findings are:

- 351 • Group means and CVs for tNAA and tCho agreed well across vendors and algorithms.
352 For mI and Glx, group means and CVs were less consistent between algorithms, with a
353 higher degree of agreement between Osprey and LCModel than with Tarquin.
- 354 • The strength of the correlations between individual metabolite estimates from different
355 algorithms was moderate. In general, tNAA and tCho estimates from different algorithms
356 agreed better than Glx and mI. With each sub-level of analysis, the variability of
357 correlation strength increased, i.e. correlations grew increasingly variable when
358 calculated separately for each vendor, or even each site.
- 359 • Overall, the association between metabolite estimates and the local baseline power was
360 significant, with mI and Glx showing stronger associations than tNAA and tCho, and
361 LCModel showing greater effects than Tarquin and Osprey.

362 The strong agreement of group means and CVs for metabolites with prominent singlets
363 (tNAA/tCho) and inconsistency for lower-intensity coupled signals (mI/Glx) are in line with pre-
364 vious two-tool comparisons of simulated data ^{7,15} and in-vivo studies with smaller sample sizes
365 ^{7,14,16}.

366 While previous work highlighted group means and standard deviations, the between-algorithm
367 agreement of individual metabolite estimates has not been extensively studied. Our results sug-
368 gest that substantial variability is introduced by the choice of the analysis software itself, indi-
369 cated by only moderate between-algorithm correlation strength (between-algorithm mean $\overline{R^2} \leq$
370 0.5 for all investigated metabolites), even for the well-established LCM algorithms LCModel and
371 Tarquin (R^2 between 0.27 and 0.59 for all metabolites). This finding raises concerns about the
372 generalizability and reproducibility of MRS study results. MRS studies typically suffer from low
373 sample sizes (~20 per comparison group is common). Considering the moderate between-tool
374 correlation of individual estimates, it is likely that marginally significant group effects and corre-
375 lations found with one analysis tool will not be found with another tool, even if the exact same

376 dataset is used. This is exacerbated by the substantial variability of correlation strengths at ven-
377 dor- or even site-level, and is even more likely to be the case for ‘real-life’ clinical data, given
378 the relatively high quality of the dataset in this study (standardized pre-processing; large sample
379 size; high SNR; low linewidth; young, healthy, cooperative subjects). While two previous studies
380 found that some differences between clinical groups remained significant independent of the
381 LCM algorithm^{14,16}, this is questionable as a default assumption. The lack of comparability aris-
382 ing from the additional variability originating in the choice of analysis tool is rarely recognized
383 or acknowledged. If choice of analysis tool is a significant contributor to measurement variance,
384 it could be argued that modelling of data with more than one algorithm will improve the
385 robustness and power of MRS studies. It should also be investigated whether the reduction of the
386 degrees of freedom by improving MM and baseline models (e.g. by using acquired MM data)
387 increases between-tool agreement and consistency between sites and vendors.

388 Sources of variance

389 In order to understand the substantial variability introduced by the choice of analysis tool, the in-
390 fluence of modelling strategies and parameters on quantitative results needs to be better under-
391 stood. Previous investigations have shown that, within a given LCM algorithm, metabolite esti-
392 mates can be affected by the choice of baseline knot spacing^{36,37}, the modelling of MM and lipids
393^{36,38}, and SNR and linewidth³⁹⁻⁴². In this study, we focused on the comparison of each LCM with
394 their default parameters, and observed differences resulting both from the default parameters and
395 from differences in the core algorithm.

396 LCM relies on the assumption that broad background and baseline signals can be separated from
397 narrower metabolite signals. This is true to a limited degree, and the choice of MM and baseline
398 modelling influences the quantification of metabolite resonances⁴. Our secondary analysis of the
399 relationship between baseline power and metabolite estimates showed a stronger interaction for
400 the broader coupled signals of Glx and mI than the singlets. tCho showed the weakest effect, and
401 the three LCMs showed the highest agreement between the MM+baseline models around 3.2
402 ppm. The higher variance of Glx and mI estimates may at least partly be explained by the ab-
403 sence of MM basis functions for frequencies >3 ppm in the model. MM signal must therefore ei-
404 ther be modelled by metabolite basis functions or the spline baseline. Including experimental
405 MM acquisitions into studies may reduce the degrees of freedom of modelling, but introduce
406 other sources of variance, such as age-dependency⁴³ or tissue composition^{38,44}. While consensus

407 is emerging that such approaches are recommended many open questions must be resolved be-
408 fore the recommendations can be broadly implemented²⁵.
409 For all three LCM algorithms, optimization between the model and the data is solved by local
410 optimization. Algorithms could converge on a local minimum, if the search space of the non-
411 linear parameters is of high dimensionality, or if the starting values of the parameters are far
412 away from the global optimum⁴⁵. The availability of open-source LCM such as Tarquin and Os-
413 prey will allow further investigation of the relationship between optimization starting values and
414 modelling outcomes.

415
416 Since this study focused on reporting tCr ratios, it is important to consider the variance of the
417 creatine model of each algorithm. With MRS only quantitative in a relative sense, separating the
418 variance contribution of the reference signal is a challenge. While mean tCr model areas were
419 slightly higher for LCModel than for Osprey and Tarquin, there was no generalizable observa-
420 tion of lower tCr ratios from LCModel. CVs of the tCr model areas were comparable across
421 LCM algorithms for each vendor. Vendor differences in water suppression of each vendor were
422 accounted for by limiting the analysis range to 0.5 to 4 ppm, and by including a -CrCH₂ correc-
423 tion term (omitted from calculations of the tCr ratios and the secondary analysis of the tCr mod-
424 els). The contribution of the reference signal to the variance of metabolite estimates is unclear
425 and hard to isolate. Nevertheless, tCr referencing was preferred in this study, since water refer-
426 encing is likely to add additional tool-specific variance resulting from water amplitude estima-
427 tion.

428

429 Limitations

430 As mentioned in greater detail above, there is currently no widely adopted consensus on the defi-
431 nition of MM basis functions, and measured MM background data are not widely available to
432 non-expert users. To reflect common practice in current MRS applications, the default MM basis
433 function definitions from LCModel were adapted for each algorithm in this study. These basis
434 functions only included MMs for frequencies < 3.0 ppm, which is likely insufficient for the mod-
435 elling of MM signals between 3 and 4 ppm⁴⁶, and will have repercussions for the estimation of
436 tCho, mI, and Glx. Second, standard modelling parameters were chosen for each LCM, which
437 ensure a broader comparability to the current literature, but may not be ideal. Third, there is

438 obviously no ‘gold standard’ of metabolite level estimation to validate MRS results against. The
439 performance of an algorithm is often judged based on the level of variance, but low variance
440 clearly does not reflect accuracy and may indicate insufficient responsiveness of a model to the
441 data. In comparing multiple algorithms, it is tempting to infer algorithms that show a higher de-
442 gree of correlation in results are more reliable, but it could equally be the case that shared algo-
443 rithm-based sources of variance increase such correlations. Efforts to use simulated spectra as a
444 gold-standard, including those applying machine learning^{47,48}, can only be successful to the ex-
445 tent that simulated data are truly representative of in-vivo data. Fourth, another criterion to judge
446 the performance of an algorithm is the residual. For example, a small residual indicates a higher
447 agreement between the complete model and the data for LCModel, it does not infer a better esti-
448 mation of individual metabolites, and may result from the higher degree of freedom in the base-
449 line of LCModel (higher number of splines) compared to Osprey and Tarquin. This is empha-
450 sized by the high agreement of the mean ml models, but lower agreement of the baseline models
451 around 3.58 ppm between LCModel and Osprey. Fifth, this study was limited to the two most
452 widely used algorithms LCModel and Tarquin, as well as the Osprey algorithm that is under on-
453 going development in our group. While including additional algorithms would increase the gen-
454 eral understanding of different algorithms, the complexity of the resulting analysis and interpre-
455 tation would be overwhelming and beyond the scope of a single publication.
456

457 **Conclusion**

458 This study presents a comparison of three LCM algorithms applied to a large short-TE PRESS
459 dataset. While different LCM algorithms' estimates of major metabolite levels agree broadly at a
460 group level, correlations between results are only weak-to-moderate, despite standardized pre-
461 processing, a large sample of young, healthy and cooperative subjects, and high spectral quality.
462 The variability of metabolite estimates that is introduced by the choice of analysis software is
463 substantial, raising concerns about the robustness of MRS research findings, which typically use
464 a single algorithm to draw inferences from much smaller sample sizes.

465

466 **Acknowledgement**

467 This work is supported by NIH grants R01 EB016089 R01 EB023963 R21A G060245. GO re-
468 ceives support from NIH grant K99 AG062230. MP is supported by NIH grants P41EB015909
469 and R01NS106292.
470

471 References

- 472 1. Öz G, Alger JR, Barker PB, et al. Clinical Proton MR Spectroscopy in Central Nervous
473 System Disorders. *Radiology*. 2014;270(3):658-679. doi:10.1148/radiol.13130531
- 474 2. Wilson M, Andronesi O, Barker PB, et al. Methodological consensus on clinical proton
475 MRS of the brain: Review and recommendations. *Magn Reson Med*. 2019;82(2):527–550.
476 doi:10.1002/mrm.27742
- 477 3. Bottomley P. *Selective Volume Method for Performing Localized NMR Spectroscopy*. Vol
478 3.; 1985. doi:10.1016/0730-725X(85)90032-3
- 479 4. Near J, Harris AD, Juchem C, et al. Preprocessing, analysis and quantification in single-
480 voxel magnetic resonance spectroscopy: experts' consensus recommendations. *NMR Bio-
481 med*. 2020;n/a(n/a):e4257. doi:10.1002/nbm.4257
- 482 5. Oeltzschner G, Zöllner HJ, Hui SCN, et al. Osprey: Open-source processing, reconstruction
483 & estimation of magnetic resonance spectroscopy data. *J Neurosci Methods*.
484 2020;343:108827. doi:10.1016/j.jneumeth.2020.108827
- 485 6. Juchem C. INSPECTOR - A Tool for Teaching Magnetic Resonance Spectroscopy. In: *26th
486 Annual Meeting of the International Society for Magnetic Resonance in Medicine (ISMRM)*.
487 Paris, France; 2018.
- 488 7. Wilson M, Reynolds G, Kauppinen RA, Arvanitis TN, Peet AC. A constrained least-
489 squares approach to the automated quantitation of in vivo 1 H magnetic resonance spectroscopy
490 data. *Magn Reson Med*. 2011;65(1):1–12. doi:10.1002/mrm.22579
- 491 8. Pouillet J-B, Sima DM, Simonetti AW, et al. An automated quantitation of short echo time
492 MRS spectra in an open source software environment: AQSES. *NMR Biomed*.
493 2007;20(5):493–504. doi:10.1002/nbm.1112
- 494 9. Soher BJ, Semanchuk P, Todd D, Steinberg J, Young K. VeSPA: Integrated applications
495 for RF pulse design, spectral simulation and MRS data analysis. In: *19th Annual Meeting of
496 the International Society for Magnetic Resonance in Medicine (ISMRM)*. Montreal, Canada;
497 2011. <https://cds.ismrm.org/protected/11MProceedings/files/1410.pdf>. Accessed May 19,
498 2020.
- 499 10. Graveron-Demilly D. Quantification in magnetic resonance spectroscopy based on semi-
500 parametric approaches. *Magn Reson Mater Phys Biol Med*. 2014;27(2):113-130.
501 doi:10.1007/s10334-013-0393-4
- 502 11. Provencher SW. Estimation of metabolite concentrations from localized in vivo proton
503 NMR spectra. *Magn Reson Med*. 1993;30(6):672–679. doi:10.1002/mrm.1910300604
- 504 12. Osorio-Garcia MI, Sima DM, Nielsen FU, Himmelreich U, Huffel SV. Quantification of
505 magnetic resonance spectroscopy signals with lineshape estimation. *J Chemom*.
506 2011;25(4):183-192. doi:10.1002/cem.1353

- 507 13. Shen ZW, Chen YW, Wang HY, et al. Quantification of Metabolites in Swine Brain by ¹H
508 MR Spectroscopy Using LCModel and QUEST: A Comparison Study. In: *2008 Congress*
509 *on Image and Signal Processing*. Vol 5. ; 2008:299-302. doi:10.1109/CISP.2008.478
- 510 14. Kossowski B, Orzeł J, Bogorodzki P, Wilson M, Setkowicz Z, P. Gazdzinski S. Follow-up
511 analyses on the effects of long-term use of high fat diet on hippocampal metabolite concen-
512 trations in Wistar rats: Comparing Tarquin quantification of 7.0T rat metabolites to
513 LCModel. *Biol Eng Med*. 2017;2(4). doi:10.15761/BEM.1000129
- 514 15. Mosconi E, Sima DM, Garcia MIO, et al. Different quantification algorithms may lead to
515 different results: a comparison using proton MRS lipid signals. *NMR Biomed*.
516 2014;27(4):431-443. doi:10.1002/nbm.3079
- 517 16. Scott J, Underwood J, Garvey LJ, Mora-Peris B, Winston A. A comparison of two post-pro-
518 cessing analysis methods to quantify cerebral metabolites measured via proton magnetic
519 resonance spectroscopy in HIV disease. *Br J Radiol*. 2016;89(1060):20150979.
520 doi:10.1259/bjr.20150979
- 521 17. Považan M, Mikkelsen M, Berrington A, et al. Comparison of Multivendor Single-Voxel
522 MR Spectroscopy Data Acquired in Healthy Brain at 26 Sites. *Radiology*.
523 2020;295(1):191037. doi:10.1148/radiol.2020191037
- 524 18. Mikkelsen M, Barker PB, Bhattacharyya PK, et al. Big GABA: Edited MR spectroscopy at
525 24 research sites. *NeuroImage*. 2017;159:32–45. doi:10.1016/j.neuroimage.2017.07.021
- 526 19. Big GABA repository. Big GABA repository. https://www.nitrc.org/projects/big_gaba/. Pub-
527 lished 2018. Accessed May 27, 2020.
- 528 20. Hall EL, Stephenson MC, Price D, Morris PG. Methodology for improved detection of low
529 concentration metabolites in MRS: Optimised combination of signals from multi-element
530 coil arrays. *NeuroImage*. 2014;86:35-42. doi:10.1016/j.neuroimage.2013.04.077
- 531 21. Klose U. In vivo proton spectroscopy in presence of eddy currents. *Magn Reson Med*.
532 1990;14(1):26–30. doi:10.1002/mrm.1910140104
- 533 22. Mikkelsen M, Tapper S, Near J, Mostofsky SH, Puts NAJ, Edden RAE. Correcting fre-
534 quency and phase offsets in MRS data using robust spectral registration. *NMR Biomed*. July
535 2020:e4368. doi:10.1002/nbm.4368
- 536 23. Barkhuijsen H, de Beer R, van Ormondt D. Improved algorithm for noniterative time-do-
537 main model fitting to exponentially damped magnetic resonance signals. *J Magn Reson*
538 *1969*. 1987;73(3):553–557. doi:10.1016/0022-2364(87)90023-0
- 539 24. Simpson R, Devenyi GA, Jezzard P, Hennessy TJ, Near J. Advanced processing and simu-
540 lation of MRS data using the FID appliance (FID-A)—An open source, MATLAB-based
541 toolkit. *Magn Reson Med*. 2017;77(1):23–33. doi:10.1002/mrm.26091

- 542 25. Cudalbu C, Behar KL, Bhattacharyya PK, et al. Contribution of macromolecules to brain
543 1H MR spectra: Experts' consensus recommendations. *NMR Biomed Revis.* 2020.
- 544 26. Provencher S. LCMModel & LCMgui User's Manual. LCMModel & LCMgui User's Manual.
545 <http://s-provencher.com/pub/LCMModel/manual/manual.pdf>. Published 2020. Accessed July
546 15, 2020.
- 547 27. Levenberg K. A method for the solution of certain non-linear problems in least squares. *Q*
548 *Appl Math.* 1944;2(2):164-168. doi:10.1090/qam/10666
- 549 28. Marquardt DW. An Algorithm for Least-Squares Estimation of Nonlinear Parameters. *J Soc*
550 *Ind Appl Math.* 1963;11(2):431-441. doi:10.1137/0111030
- 551 29. R Core Team. *R: A Language and Environment for Statistical Computing.* Vienna, Austria:
552 R Foundation for Statistical Computing; 2017. <https://www.R-project.org/>.
- 553 30. SpecVis GitHub repository. SpecVis GitHub repository.
554 <https://github.com/hezoe100/SpecVis>. Published 2020. Accessed May 27, 2020.
- 555 31. Zöllner HJ. Comparison of algorithms for linear-combination modelling of short-echo-time
556 magnetic resonance spectra. <https://osf.io/3ekq4/>. Published June 1, 2020. Accessed June 2,
557 2020.
- 558 32. <https://github.com/martin3141/spant>. spant GitHub repository. [https://github.com/mar-](https://github.com/martin3141/spant)
559 [tin3141/spant](https://github.com/martin3141/spant). Published 2017. Accessed May 27, 2020.
- 560 33. Allen M, Poggiali D, Whitaker K, Marshall TR, Kievit RA. Raincloud plots: a multi-plat-
561 form tool for robust data visualization. *Wellcome Open Res.* 2019;4:63. doi:10.12688/well-
562 comeopenres.15191.1
- 563 34. Wickham H. *Ggplot2: Elegant Graphics for Data Analysis.* Springer-Verlag New York;
564 2009. <http://ggplot2.org>.
- 565 35. Fagerland MW. T-tests, non-parametric tests, and large studiesa paradox of statistical prac-
566 tice? *BMC Med Res Methodol.* 2012;12(1):78. doi:10.1186/1471-2288-12-78
- 567 36. Marjańska M, Terpstra M. Influence of fitting approaches in LCMModel on MRS quantifica-
568 tion focusing on age-specific macromolecules and the spline baseline. *NMR Biomed.* No-
569 vember 2019. doi:10.1002/nbm.4197
- 570 37. Wenger KJ, Hattingen E, Harter PN, et al. Fitting algorithms and baseline correction influ-
571 ence the results of non-invasive in vivo quantitation of 2-hydroxyglutarate with 1H-MRS.
572 *NMR Biomed.* 2019;32(1):e4027. doi:10.1002/nbm.4027
- 573 38. Schaller B, Xin L, Gruetter R. Is the macromolecule signal tissue-specific in healthy human
574 brain? A ¹H MRS study at 7 tesla in the oc-
575 cipital lobe. *Magn Reson Med.* 2014;72(4):934–940. doi:10.1002/mrm.24995

- 576 39. Bartha R. The Effect of Signal to Noise Ratio and Linewidth On 4T Short Echo Time 1H
577 MRS Metabolite Quantification. *Proc 13th Sci Meet Int Soc Magn Reson Med.*
578 2005;216(1):2459–2459.
- 579 40. Near J. Investigating the effect of spectral linewidth on metabolite measurement bias in
580 short-TE MRS. In: *21th Annual Meeting of the International Society for Magnetic Reso-*
581 *nance in Medicine (ISMRM).* Milan, Italy; 2014.
- 582 41. Wijtenburg SA, Knight-Scott J. The Impact of SNR on the Reliability of LCModel and
583 QUEST Quantitation in 1 H-MRS. In: *17th Annual Meeting of the International Society for*
584 *Magnetic Resonance in Medicine (ISMRM).* ; 2009.
- 585 42. Zhang Y, Shen J. Effects of noise and linewidth on in vivo analysis of glutamate at 3 T. *J*
586 *Magn Reson.* 2020;314. doi:10.1016/j.jmr.2020.106732
- 587 43. Marjańska M, Deelchand DK, Hodges JS, et al. Altered macromolecular pattern and con-
588 tent in the aging human brain. *NMR Biomed.* 2018;31(2):e3865. doi:10.1002/nbm.3865
- 589 44. Považan M, Strasser B, Hangel G, et al. Simultaneous mapping of metabolites and individ-
590 ual macromolecular components via ultra-short acquisition delay 1H MRSI in the brain at
591 7T. *Magn Reson Med.* 2018;79(3):1231-1240. doi:10.1002/mrm.26778
- 592 45. Pouillet J-B, Sima DM, Van Huffel S. MRS signal quantitation: A review of time- and fre-
593 quency-domain methods. *J Magn Reson.* 2008;195(2):134-144.
594 doi:10.1016/j.jmr.2008.09.005
- 595 46. Giapitzakis I-A, Avdievich N, Henning A. Characterization of macromolecular baseline of
596 human brain using metabolite cycled semi-LASER at 9.4T. *Magn Reson Med.*
597 2018;80(2):462-473. doi:10.1002/mrm.27070
- 598 47. Lee HH, Kim H. Deep learning-based target metabolite isolation and big data-driven meas-
599 urement uncertainty estimation in proton magnetic resonance spectroscopy of the brain.
600 *Magn Reson Med.* 2020;n/a(n/a). doi:10.1002/mrm.28234
- 601 48. Lee HH, Kim H. Intact metabolite spectrum mining by deep learning in proton magnetic
602 resonance spectroscopy of the brain. *Magn Reson Med.* 2019;82(1):33-48.
603 doi:10.1002/mrm.27727
- 604

Figure Captions

Figure 2. Overview of the MRS analysis pipeline. (A) Pre-processing pipeline implemented in Osprey including ‘OspreyLoad’ to load the vendor-native spectra, ‘OspreyProcess’ to process the raw data and to export the averaged spectra. (B) Modelling of the averaged spectra with details of the basis set and parameters of each LCM (LCModel, Osprey, and Tarquin).

Figure 2. Summary of the modelling results. (A–C) site-level averaged residual, data, model, MM model + baseline, baseline and MM model for each LCM algorithm, color-coded by vendor. (D–F) cohort-mean residual, data, model, MM model + baseline, and metabolite models for each vendor, color-coded by LCM algorithm.

Figure 3. – Metabolite level distribution. Raincloud plots of the metabolite estimates of each LCM algorithm (color-coded). The four metabolites are reported in the columns, and the three vendors in rows, with a cohort summary in the last row. The coefficient of variation is reported for each distribution, as well as a mean \overline{CV} reported in the last column, which is calculated across each row. Asterisks indicate significant differences (adjusted $p < 0.001 = ***$).

Figure 4. Pairwise correlational comparison of algorithms. LCModel and Osprey are compared in the first row, Tarquin and Osprey in the second row, and LCModel and Tarquin in the third row. Each column corresponds to a different metabolite. Within-vendor correlations are color-coded; global correlations are shown in black. The $\overline{R^2}$ values are calculated along each dimension of the grid with mean R^2 for each metabolite and each correlation. A cohort-mean $\overline{R^2}$ value is also calculated across all twelve pair-wise correlations. Asterisks indicate significant correlations ($p < 0.01 = **$ and $p < 0.001 = ***$).

Figure 5. Correlation analysis between metabolite estimates and local baseline power for each algorithm, including global (black) and within-vendor (color-coded) correlations. The mean $\overline{R^2}$ values are calculated along each dimension of the grid for each metabolite and each algorithm. Similarly, a cohort-mean $\overline{R^2}$ value is calculated across all twelve pair-wise correlations. Asterisks indicate significant correlations ($p < 0.05 = *$, $p < 0.01 = **$, $p < 0.001 = ***$).

Figure 6. Variability of tCr models. Mean models +/- standard deviation (shaded areas) are presented column-wise by vendor and color-coded by LCM algorithm. The distribution and CV of the areas under the models are inset.

Supplementary Material 3. *Facetted pair-wise correlational comparison of algorithms. LCModel and Osprey are compared in the first row, Tarquin and Osprey are compared in the second row, and LCModel and Tarquin are compared in the third row. Each sub-plot (A-D) corresponds to a different metabolite. Within-vendor (bold line with confidence interval) and within-site (thin line) correlations are color-coded. Asterisks indicate significant correlations ($p < 0.01 = **$ and $p < 0.001 = ***$).*

Table Captions

Table 3. Overview of linear-combination modelling algorithms. The domain (time TD or frequency FD) of modelling and the baseline model approach are specified. *Citations reported from Google Scholar on July 29, 2020.

Table 4. Metabolite level distribution. Mean, standard deviation and coefficient of variation (CV) of each metabolite-to-creatine ratio, listed by algorithm and vendor as well as global summary values. Asterisks indicate significant differences (adjusted $p < 0.01 = **$ and adjusted $p < 0.001 = ***$ or #### or '') in the mean (for the metabolite ratios) or the variance (for the CV) compared to the algorithm in the next row (LCModel vs Osprey = ** or ***, Osprey vs Tarquin = ####, and Tarquin vs LCModel = '').

Supplementary Material 1. Properties of the Gaussian functions of the broad macromolecule and lipid resonances included in the basis sets, taken from section 11.7 of the LCModel manual. The amplitude values are scaled relative to the CH₃ singlet of creatine with amplitude 3.

Supplementary Material

<i>Name</i>	<i>Frequencies [ppm]</i>	<i>FWHM [ppm]</i>	<i>Amplitude</i>
MM09	0.91	0.14	3.00
MM12	1.21	0.15	2.00
MM14	1.43	0.17	2.00
MM17	1.67	0.15	0.20
MM20	2.08	0.15	1.33
	2.25	0.20	0.33
	1.95	0.15	0.33
	3.00	0.20	0.40
Lip09	0.89	0.14	3.00
Lip13a	1.28	0.15	2.00
Lip13b	1.28	0.089	2.00
Lip20	2.04	0.15	1.33
	2.25	0.15	0.67
	2.80	0.20	0.87

Supplementary Material 1. Properties of the Gaussian functions of the broad macromolecule and lipid resonances included in the basis sets, taken from section 11.7 of the LCModel manual. The amplitude values are scaled relative to the CH₃ singlet of creatine with amplitude 3.

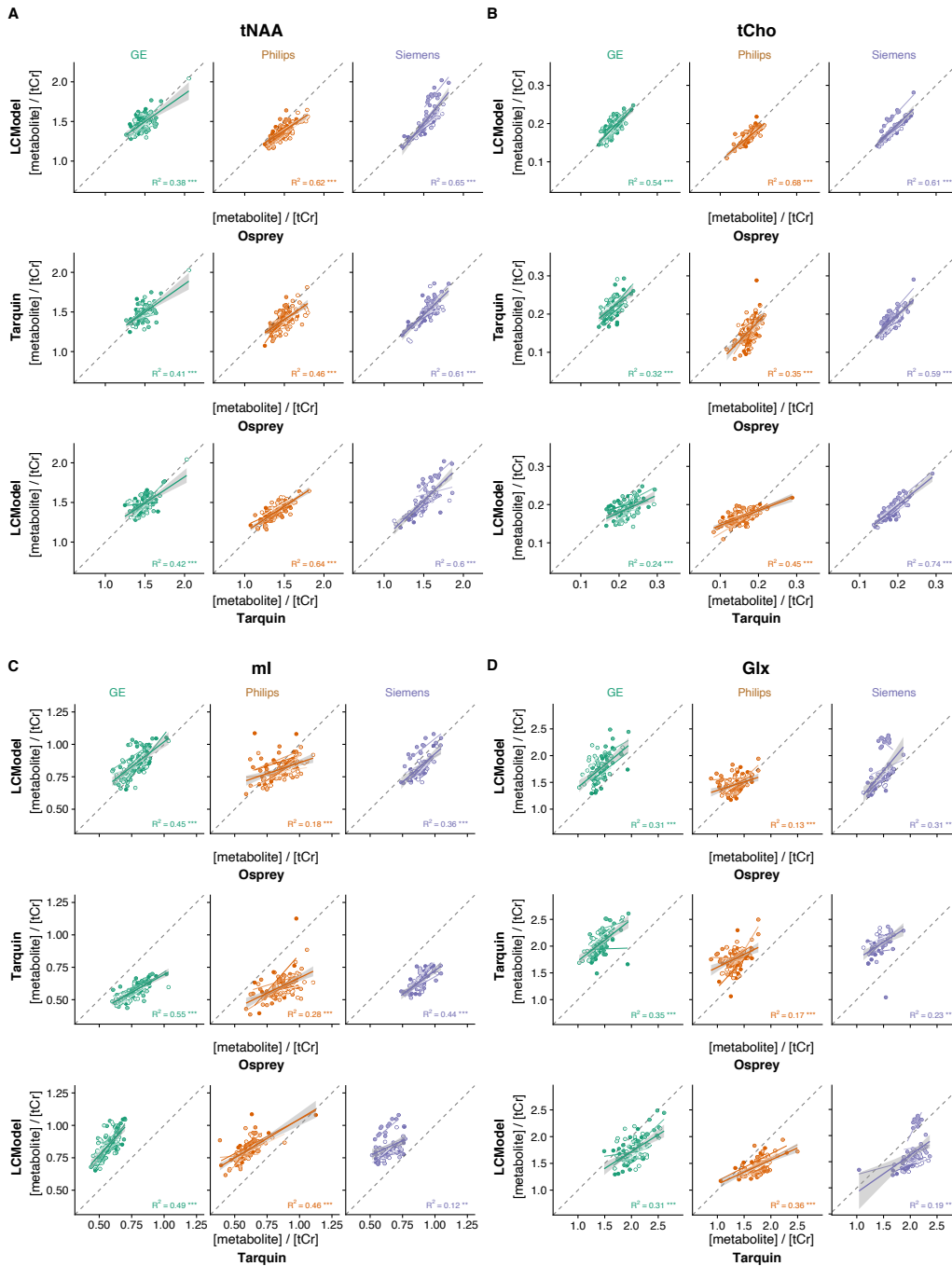
Supplementary Material 2 – Overview plot and secondary analyses

Details on the creation of the visual overview plot

As in the default visualizations for the LCModel and Tarquin software interfaces, inverse phase estimates were applied to the spectra and final models. For the visualization, spectra were normalized to the amplitude of the 3-ppm creatine singlet, and a DC offset was added to each site mean spectrum to align the mean frequency-domain amplitude between 1.85 and 4.0 ppm, to aid visual comparison between algorithms and sites.

Details on the three secondary analyses:

1. To investigate potential vendor differences in linewidth and SNR based on the different export formats of the data, NAA linewidth and SNR were investigated.
2. To investigate potential interactions between baseline power and metabolite estimates unbiased by DC offsets, the MM + baseline models were first aligned vertically according to the frequency-domain minimum of the acquired spectra between 2.66 and 2.7 ppm (i.e. between the aspartyl signals, which is the region with the highest consistency between the baseline models). Baseline models were normalized to the frequency-domain amplitude of each metabolite spectrum between 2.9 and 3.1 ppm to account for differences in the scaling of the model outputs of LCModel and Tarquin. Baseline power beneath each major metabolite was then defined as the range-normalized integral of the baseline model between 1.9 and 2.1 ppm for the tNAA baseline; 3.1 and 3.3 ppm for the tCho baseline; 3.33 and 3.75 ppm for mI; and 1.9 to 2.5 ppm and 3.6 to 3.8 ppm for the Glx baseline.
3. The contribution of variance in modelling of the creatine reference signal to metabolite ratios was also investigated. To this end, each individual total creatine model (Cr + PCr) was normalized to the frequency-domain amplitude of each metabolite spectrum between 1.9 and 2.1 ppm to account for differences in the scaling of the total creatine model outputs of LCModel and Tarquin. Finally, the integral over the individual creatine model was calculated.



Supplementary Material 3. Facetted pair-wise correlational comparison of algorithms. LCMoDel and Osprey are compared in the first row, Tarquin and Osprey are compared in the second row, and LCMoDel and Tarquin are compared in the third row. Each sub-plot (A-D) corresponds to a different metabolite. Within-vendor (bold line with confidence interval) and within-site (thin line) correlations are color-coded. Asterisks indicate significant correlations ($p < 0.01 = **$ and $p < 0.001 = ***$).